This is the peer-reviewed, final accepted version for American Mineralogist, published by the Mineralogical Society of America.
The published version is subject to change. Cite as Authors (Year) Title. American Mineralogist, in press.
DOI: https://doi.org/10.2138/am-2021-7765. http://www.minsocam.org/

Revision 3

Word Count: 8284

High-pressure synchrotron single crystal X-ray diffraction study of lillianite.

Azzurra Zucchini 1*, Tonci Balić-Žunić 2, Ines E. Collings 3, Michael Hanfland 3, Paola Comodi 1

1 Dipartimento di Fisica e Geologia, Università di Perugia, 06123 Perugia, Italy; azzurra.zucchini@unipg.it (A.Z.); paola.comodi@unipg.it (P.C.)

2 Department of Geosciences and Natural Resource Management, University of Copenhagen, 1350 Copenhagen, Denmark; toncib@ign.ku.dk (T.B.Z.)

3 European Synchrotron Radiation Facility, 71 avenue des Martyrs, 38000 Grenoble, France; hanfland@esrf.fr (M.H.); ines.collings@esrf.fr (I.C.)

* Correspondence: azzurra.zucchini@unipg.it; Tel.: +39-075-5852614

Abstract

In the present paper, high pressure data from a synchrotron X-ray diffraction study on a lillianite ($Pb_3Bi_2S_6$) single crystal up to approximately 21 GPa are presented.

A phase transition from lillianite (*Bbmm* space group #63, L*P* lillianite) to the high-pressure form *β*-$Pb_3Bi_2S_6$ (*Pbnm* space group, H*P* lillianite) was confirmed and bracketed between 4.90 and 4.92 GPa. The transition is reversible but of first-order with a hysteresis of ~2.8 GPa. The phase transition to *β*-$Pb_3Bi_2S_6$ showed weak effects of pseudomerohedral twinning that disappeared upon decompression, testifying to a full recovery of the single crystal of lillianite. This makes lillianite an interesting shape-memory material.

With a bulk modulus $K_{4.9}$ = 78(3) GPa and K' = 5.1(4), *β*-$Pb_3Bi_2S_6$ is markedly less compressibile than lillianite [K_0 = 44(2) GPa, K' = 7(1)]. Compressional anisotropy increased markedly in *β*-$Pb_3Bi_2S_6$ with compressibility along the *b* axis [M_{0b} = 130(6) GPa and M'_b = 19(3) in lillianite, $M_{4.9b}$ = 145(4) GPa and

This is the peer-reviewed, final accepted version for American Mineralogist, published by the Mineralogical Society of America.
The published version is subject to change. Cite as Authors (Year) Title. American Mineralogist, in press.
DOI: https://doi.org/10.2138/am-2021-7765. http://www.minsocam.org/

M'_b = 16.0(7) in β-$Pb_3Bi_2S_6$] significantly larger than along the other two axes [M_{0a} = 118(5) GPa, M'_a = 21(3), M_{0c} = 139(12) GPa and M'_c = 31(10) in lillianite, $M_{4.9a}$ = 242(12) GPa, M'_a = 8(1), $M_{4.9c}$ = 242(5) GPa and M'_c = 29(1) in β-$Pb_3Bi_2S_6$].

The behavior of lillianite at high pressure is an interesting case study in relation to non-quenchable ultra-high-pressure phases likely occurring in the inner Earth, like post-perovskite $MgSiO_3$, the oxide homologue N = 1 of the lillianite series. The β-$Pb_3Bi_2S_6$ structure, on the other hand, is the N = 3 homologue of the meneghinite series where also the higher-pressure modification of the post-perovskite structure belongs (homologue N = 1). This makes the two forms of $Pb_3Bi_2S_6$ potential equivalents of high- and ultra-high-pressure Mg silicates that could occur both in the deep earth mantle and in other rocky extrasolar planetary bodies.

Keywords

Lillianite; high-pressure; synchrotron; single crystal X-ray diffraction; phase transition; shape-memory

This is the peer-reviewed, final accepted version for American Mineralogist, published by the Mineralogical Society of America.
The published version is subject to change. Cite as Authors (Year) Title. American Mineralogist, in press.
DOI: https://doi.org/10.2138/am-2021-7765. http://www.minsocam.org/

Introduction

During the last decades, the crystal structure and stability of main-group heavy metal chalcogenides have attracted the interest of the scientific community as likely candidates for renewable energy applications (Olvera et al. 2015 and references therein). In particular, sulfosalts have been claimed as promising materials able to both absorb sunlight more efficiently than silicon (Wallace et al. 2017) and to avoid the toxicity issues found with the lead- and tin-halide perovskite (Kanno et al. 2019) in the thin-film solar cells technology. Sulfosalts are complex sulfides of As, Sb and Bi with one or more metal cations. Because of the presence of the s^2 lone electron pair (LEP) of the trivalent metalloids together with the nature of the metalloids-sulfur bond, sulfosalts have specific semiconducting properties (Olsen et al. 2008).

Some of the sulfosalts investigated at high-pressure showed interesting pressure-induced structural phase transitions, e.g. heyrovskyite $Pb_6Bi_2S_9$ (Olsen et al. 2011) and chalcostibite $CuSbS_2$ (Comodi et al. 2018). Pressure appears to be an important parameter, which could be used to either tune or significantly change the transport and structural properties of these thermoelectric materials.

The crystal structure of lillianite (Takagi and Takéuchi 1972; Figure 1a) consists of (010) slabs that have internal topology of a NaCl(PbS)-type. The boundary of slabs is cut along the {311} planes of the PbS archetype. The neighboring slabs are in a twin relation relative to their boundary. The crystal structure is characterized by two relatively long periods (along *b* axis perpendicular to slabs, and along *a* axis corresponding to [2-3-3] direction of the PbS archetype, respectively) and one short period along *c* axis matching the [011] direction of the PbS archetype. The symmetry elements of the PbS archetype that remain parallel in both orientations of slabs are the two-fold axes along the $[011]_{PbS}$ and the mirror planes perpendicular to them, that is, the *c* axis and the (001) plane in the lillianite crystal structure, respectively. The structure contains three distinct metal sites, M1, M2 and M3 as shown in Figure 1a. Based on the

bond distances, M3 site is fully occupied by Pb, whereas M1 and M2 sites have a mixed (Pb,Bi) occupancy with a likely preference for Bi in M1 and for Pb in M2 (Pinto et al. 2006). Due to their similar and high atomic numbers, it is not possible to refine the amounts of Bi and Pb in the mixed sites from X-ray diffraction data. Therefore, various authors used a fixed 1:1 occupancy of Bi and Pb on M1 and M2 sites in lillianite crystal structure refinements (Takagi and Takeuchi 1972; Olsen et al. 2008). Lillianite has an ordered polymorph, the monoclinic *C2/m* xilingolite (Berlepsch et al. 2001a). The main difference is that in a slab M1 sites are occupied predominantly with Pb and the M2 sites with Bi, whereas in a successive slab the situation is reversed. In other words, all slabs with the same inclination of atomic planes have Bi predominantly occupying M1, whereas the slabs with the opposite inclination have Bi dominating in M2.

Lillianite is a part of a homologous series where all members share the described topological features but differ in the thicknesses of slabs. The standard classification of the lillianite homologues (Makovicky 1977) defines the thicknesses of the slabs through the number of the coordination octahedra in a row running across the slab along the [100] direction of the PbS archetype. In the standard notation that takes into consideration the existence of homologues with two slabs of different thicknesses, lillianite is the ^{4,4}L member of the series, meaning that it has four octahedra in a row across the slab for both slabs that are in a twin relation. In the case of homologues with slabs of equal thicknesses, their boundaries are also mirror planes of the crystal structure, which, combined with the earlier mentioned symmetry elements, results in an overall orthorhombic symmetry (*Bbmm* space group #63).

In the pressure range between 3.7 and 4.9 GPa lillianite has been shown to undergo a phase transition with a volume decrease of approximately 4% (Olsen et al. 2008). The crystal structure of the β-$Pb_3Bi_2S_6$ is shown in Figure 1b. In β-$Pb_3Bi_2S_6$, *n*-glide planes replace the mirror planes perpendicular to the *b*-axis present in the low-pressure form. The result of the phase transition is a lowering of symmetry from *Bbmm* in lillianite (L*P* polymorph) to *Pbnm* space group in β-$Pb_3Bi_2S_6$ (H*P* polymorph), and an increase in the

number of independent atomic positions from 10 to 22. The PbS-like slabs in lillianite split in β-$Pb_3Bi_2S_6$ by means of crystallographic shear into double layer rods that extend along the *c* axis. The rods are rotated around their central 2_1 axes, reducing the inclination angle of their longest diameter to the *b* axis, which leads to an expansion in the *b*-axis direction and a contraction in the *a*-axis direction. The rotation is connected to a sliding of the adjacent rods with a relative movement between two parallel rods corresponding to half a coordination octahedron diameter or the sliding component $[0\ ½\ ½\ ]_{PbS}$.

The L*P* and H*P* polymorphs are substantially different in terms of the archetypal structure, which is PbS-like in lillianite and SnS-like in β-$Pb_3Bi_2S_6$, with an obviously larger stereochemical activity of the LEPs of M atoms in the latter (Olsen et al. 2008). Accordingly, β-$Pb_3Bi_2S_6$ structurally belongs to the meneghinite homologous series (Olsen et al. 2008). Due to the lowering of symmetry on phase transition, some of the symmetry equivalent atomic sites in lillianite split in two symmetry-independent sites in β-$Pb_3Bi_2S_6$. The here used labeling of atomic sites in β-$Pb_3Bi_2S_6$ is different from what Olsen et al. (2008) used in order to ease the comparison between the L*P* and H*P* forms of $Pb_3Bi_2S_6$. In our notation, all sites in β-$Pb_3Bi_2S_6$ retain the same numeric descriptors as the corresponding sites in lillianite and the split sites get additionally either A or B descriptors. The sites related to M1 in lillianite get labels M1A and M1B in β-$Pb_3Bi_2S_6$ etc. The reader can consult Table S1 in *Supplementary material* section for the relations between the present and Olsen et al. (2008) site notations for β-$Pb_3Bi_2S_6$.

In this work, we extended the investigated pressure range up to ~21 GPa. The new data allow us to determine the Equation of State of the β-$Pb_3Bi_2S_6$. Moreover, the crystal structure of the H*P* lillianite polymorph is revised and accurately described by collecting several high-resolution data both during compression and decompression. With the present results, the reversibility as well as the shape-memory character of the phase transition is further clarified.

Materials and methods

Data collection and extraction

The examined sample was a single lillianite crystal ($31 \times 12 \times 10$ μm^3), optically clear at 10 μm thickness, coming from the same synthesis as the crystals used by Olsen et al. (2008). The crystal quality was checked by means of in-house Single Crystal X-Ray Diffraction (SC-XRD) analysis at the Department of Physics and Geology of the University of Perugia (Italy) confirming the sharpness of the diffraction profiles and the lack of twinning.

The H*P* SC-XRD study was carried out at the ID-15B beamline at ESRF (Grenoble) by means of a membrane-type Diamond Anvil Cell with an opening angle of 64 degrees, equipped with 600 μm culet diamonds. Helium was used as a pressure transmitting medium and a Ruby sphere was loaded as a fluorescent *P* calibrant together with the samples. The pre-indented stainless-steel gasket had 300 μm diameter hole and 80 μm thickness.

A fixed monochromatized X-ray beam ($\lambda = 0.41125$ Å) was used, focused down to 10×10 μm^2 area. Data were collected with angular step of 0.5° and counting time of 1s per step and registered by means of a MAR555 flat panel detector with 430×350 mm^2 (555mm diagonal) active area. Both the sample-to-detector distance (279.88 mm) and the wavelength were calibrated using Si standard and Fit2D software (Hammersley et al. 1996).

Pressure was varied in the range from 0 to approximately 21 GPa. Measurements were performed in 10 steps on increasing pressure and 5 steps during decompression to evaluate the reversibly and the likely occurrence of hysteresis phenomena. Pressure was measured before and after each data collection and the gasket-relaxation was ensured by waiting approximately 15 minutes after changing the load.

The data extraction together with the reflection intensity correction, the merging of reflections and the refinements of the crystal lattice parameters were done by means of the CrysAlisPro software (Agilent Technologies UK Ltd, Yarnton, England.). The absorption correction of the extracted data was applied in two steps: in the first one, by means of the multi-scan method (Blessing 1995) as implemented in

WinGX (Farrugia 1999). The correction factors for intensities were optimized without assuming any physical cause like absorption. In the second step, the ABSORB-GUI software (Angel and Gonzalez-Platas 2013) was used to correct for DAC absorption and gasket shadowing.

Compressibility calculations

The compressibility of the L*P* and the H*P* lillianite phases was calculated from measured unit cell parameters. The data treatment and Equation of State (EoS) calculations were done using EosFit GUI (Gonzalez-Platas et al. 2016). The behavior of unit cell parameters with *P* for both lillianite and *β*-$Pb_3Bi_2S_6$ is shown in Figure 2 together with data from Olsen et al. (2008). Results of the EoS calculation are given in Table 1. We calculated the compressibility parameters of both lillianite and *β*-$Pb_3Bi_2S_6$ using combined data of our measurements and those published by Olsen et al. (2008) for their crystal *lill2*. Due to the hysteresis effects and lower quality of refinements, our data obtained during decompression, were not used for the calculations.

Structure refinements and analysis

The structure refinements were performed starting from the crystal structures published in Olsen et al. (2008) based on F^2 by using ShelXle software (Hübschle et al. 2011) and the scattering factors for neutral atoms.

Given the similar atomic numbers of the heavy Bi and Pb atoms, their mixed occupancies in M1 and M2 in lillianite as well as M1A, M1B, M2A and M2B in *β*-$Pb_3Bi_2S_6$ were fixed to 0.5 during refinement. Insights on the likely proportion of Bi in the mixed sites were attempted by applying the model of Brown and Altermatt (1985) for the relation bond length – bond valence and assuming the following relation:

$$xv_{i1} + (1\text{-}x)v_{i2} = xv_{c1} + (1\text{-}x)v_{c2},$$

where x is the proportion of the first species, v_{i1} and v_{i2} are the expected valences of the first and the second species, and v_{c1} and v_{c2} are valences calculated for the site using the bond valence constants for

the first and the second species, respectively. Further details on the used procedure are given in the *Supplementary material* section together with the obtained results.

Anisotropic thermal parameters were refined for Pb, Bi and S atomic positions at each pressure, with the exception of the first data collection after the phase transition (6.3 GPa) as well as data collections of β-$Pb_3Bi_2S_6$ during decompression, where thermal parameters for sulfur atoms were refined isotropically.

The good crystallinity of the lillianite crystal was maintained during the whole experiment. After the phase transition, the appearance of additional weak reflections was interpreted as twinning induced by the phase transition. This observation is supported by a successful indexing of the additional reflections using the unit cell parameters obtained from the main reflections. In Figure S1, in the *Supplementary material* section, the reciprocal lattice images for the crystal at 1.74 GPa (single lillianite crystal), 6.30 GPa (twinned *β*-$Pb_3Bi_2S_6$) and 2.13 GPa during decompression (the detwinned single lillianite crystal) are shown. Twinning persisted both during compression and decompression of the H*P* lillianite phase; whereas it disappeared after the low-pressure phase recovery. The attempted twin refinements resulted in inferior R factors compared to single-domain refinements, because the mass proportion of the second component refined to only 6%. Therefore, we used only the reflections of the main twin component for the crystal structure analysis.

The details of data collection and refinement, together with the crystal structure data, can be found in the CIF file (deposited). Bond lengths and polyhedral volumes at different pressures, are reported in Table S2 and S3 in the *Supplementary material* section, for the L*P* and the H*P* lillianite, respectively.

To calculate the deviations of atomic positions in *β*-$Pb_3Bi_2S_6$ from those of L*P* lillianite, we used the program AMPLIMODES (Orobengoa et al. 2009) from the Bilbao Crystallographic Server (https://www.cryst.ehu.es/). The calculations were made comparing the crystal structure data of lillianite at 1 MPa and 4.9 GPa with those of *β*-$Pb_3Bi_2S_6$ at 6.3 GPa. Comparing the data for lillianite for both room pressure and right before the phase transition to those of *β*-$Pb_3Bi_2S_6$, gives us a possibility also to

follow the changes in the structure of lillianite over its stability range by subtracting the two results (see further explanation below, paragraph "Crystal structure evolution with pressure"). The results are represented in Table 2.

Moreover, the distortion of coordination polyhedra was analyzed with a help of program Ivton (Balić Žunić and Vicković 1996). Three parameters were taken into account for which a prerequisite is a calculation of the best-fitting circumscribed sphere to the coordination polyhedron (Balić Žunić and Makovicky 1996): (i) eccentricity (Balić Žunić and Makovicky 1996) (ii) asphericity (Balić Žunić and Makovicky 1996; Balić-Žunić 2007) and (iii) volume distortion (Makovicky and Balić-Žunić 1998). Results are given the *Supplementary material* section (Figure S2).

Results and discussion

Compressibility

A discontinuity was observed after 4.9 GPa with a decrease of the *a* parameter (Figure 2b) and an increase of the *b* parameter (Figure 2b) of approximately 16% and 14%, respectively, in agreement with data published by Olsen et al. (2008). The evolution of cell parameters led to a decrease of the unit cell volume on phase transition from 1057.16(6) to 1006.70(6) $Å^3$ corresponding to approximately 5%.

The well covered *P* range both in the lillianite field, thanks to the combination of our compression results and those of Olsen et al. (2008) obtained from their second crystal labelled *lill2*, and in the β-$Pb_3Bi_2S_6$ field up to ~21 GPa, allowed us to accurately calculate the EoS for both phases. A comparison of the compressional behavior of the two polymorphs, together with data from Olsen et al. (2008), is given in Figure 3 where confidence ellipses are built according to Bass et al. (1981). A negative correlation between K_0 and K' is observed for both lillianite and β-$Pb_3Bi_2S_6$ as the marked elongation of the ellipses with a negative slope. The present data showed that lillianite is more compressible with a higher first derivative than what suggested by Olsen et al. (2008) (Table 1, Figure 3); whereas, the remarkably

smaller bulk compressibility of β-$Pb_3Bi_2S_6$ than that of lillianite at the transition pressure, as proposed by Olsen et al. (2008), is confirmed (Table 1, Figure 3). Our improved data show an even larger bulk modulus for the high-pressure polymorph with a smaller first derivative meaning that the compressibility of the H*P* lillianite polymorph remains almost the same in the investigated pressure range. The poor agreement of the presented data with those from Olsen et al. (2008) is likely due to insufficient data statistics caused by the restricted *P* range that was analyzed by the latter.

By the present data the axial moduli were also calculated for both L*P* and H*P* polymorphs (Table 1). Results showed that in lillianite the *a* axis is the most compressible one, whereas in β-$Pb_3Bi_2S_6$ the *b* parameter is markedly more compressible than *a*. The *c* parameter is the least compressible in both polymorphs with remarkably higher *M*' value expressing a marked stiffening as pressure increases. Further discussions on the anisotropic compressional behavior of lillianite and in β-$Pb_3Bi_2S_6$ are given below (see paragraph "Anisotropic compression in L*P* and H*P* lillianite structures").

Crystal structure evolution with pressure

The indexation of the collected reflections showed that the phase transition from lillianite to β-$Pb_3Bi_2S_6$ occurs at a pressure higher than 4.9 GPa. Together with the previous results of Olsen et al. (2008), this helps to bracket the phase transition to a very narrow range between 4.90 and 4.92 GPa. The evolution of the crystal structure during decompression showed that the β-$Pb_3Bi_2S_6$ completely reverses to the low-pressure lillianite, with hysteresis since we observed that β-$Pb_3Bi_2S_6$ remained stable during decompression down to 4.30 GPa and the reverse phase transition occurred between 4.30 and 2.13 GPa (Figure 2). Therefore, the phase transition is confirmed to be of first order, strongly anisotropic. It is reversible (Olsen et al. 2008) and involves a hysteresis behavior (present data).

Phase transition of lillianite revisited. The availability of crystal structure data over a significantly increased range of pressures, allowed a deep discussion of the lillianite behavior.

This is the peer-reviewed, final accepted version for American Mineralogist, published by the Mineralogical Society of America.
The published version is subject to change. Cite as Authors (Year) Title. American Mineralogist, in press.
DOI: https://doi.org/10.2138/am-2021-7765. http://www.minsocam.org/

Displacements of atoms upon the transition are small but indicative, as follows. S2 that lies on the two-fold axis keeps its position unchanged in accordance with the symmetry constraints (2/*m*). Inside its coordination, M3 site moves towards the plane defined by the four S4 atoms and away from the S3 atoms. The latter move in the opposite direction further increasing their distance to M3. S1 atoms (capping atoms of the trigonal prism) move towards the (010) *m* symmetry plane and M3. M2 moves towards the coordinated S1 on the same *z* level thus shortening its longest bond. M1 atoms move in approximately the same direction as the S4 atoms to which they are bonded. All these changes are a prelude to the phase transition, during which the displacements of atoms from the positions in the low-pressure phase are tremendously emphasized, some of them exceeding 1.5 Å (e.g. $|\Delta|_{M1B}$ = 1.5304 Å and $|\Delta|_{S4B}$ = 1.5845 Å, see Table 2). They are illustrated on Figure 4 and Table 2 where the active modes in both lillianite and β-$Pb_3Bi_2S_6$ are shown to be Δ_x and Δ_y. The strains accumulated during compression of lillianite are released upon transition with the spontaneous movement of atomic sites that break the *Bbmm* symmetry. Site M3, which before the phase transition was approaching S4 atoms, now changes the direction of displacement and moves away from the former mirror plane, becoming a part of a rigid rod. As a consequence, its coordination changes drastically. The body of its bicapped trigonal prism (prism axis parallel *c*) is made of two S3 and four S4 atoms, either before and after the transition. The two caps are the two S1 atoms in lillianite. In β-$Pb_3Bi_2S_6$, one of them (S1A) is displaced far away from M3 and out of the coordination, being $|\Delta|_{S1'}$ = -0.0285 and $|\Delta|_{M3}$ = 0.0059 in lillianite, $|\Delta|_{S1A}$ = 0.6511 and $|\Delta|_{M3}$ = 1.0038 in β-$Pb_3Bi_2S_6$ (Table 2); whereas, M3 moves in the direction of the other (S1B) (Table 2, $|\Delta|_{S1}$ = 0.0511 in lillianite and $|\Delta|_{S1B}$ = 1.0887in β-$Pb_3Bi_2S_6$). An additional S3 atom approaches M3 and now forms the second cap on the face formed by two S4A and two S4B atoms. This functions as a rotation of the coordination hole, especially illustrative if we consider the coordination as a square antiprism as suggested by the volume distortion parameter (Figure S2c). Differently from Olsen et al. (2008) where the approaching of the additional S3 atom was ignored and the coordination of the M3 in β-$Pb_3Bi_2S_6$ was

considered as seven-fold, here we consider the coordination as eight-fold, given that it resides in the hole made by eight S atoms. The movements of M3 sites are in the [100] direction for the sites close to the same (010) plane and in the opposite direction [-100] in the successive (010) plane (Figure 4). The side movement from the common (010) plane is successively to the opposite directions for sites close to the same (010) plane, so that M3 atoms become parts of the rigid rods in the slabs to the left and to the right of the bordering (010) plane, respectively.

The coordination of the M1 and M2 sites changes from octahedral into lying mono-capped trigonal prismatic (or a split octahedron). The lone electron pairs of M1 and M2 atoms point in the resulting structure between the rigid rods. This means that some of them moved to the other side of the M atoms during the phase transition. The coordination number changes for M1 and M2 from 6 in lillianite to 7 in β-$Pb_3Bi_2S_6$ (M1A-M1B and M2A-M2B). Although the structural change guided by the phase transition produces the same coordination type for atoms M2A, M2B, M1A and M1B – CN7 in the form of a split octahedron – the movements of atoms that result in this coordination and the changes in bonding compared to the L*P* lillianite phase are different for the atoms that now form the pairs of symmetrically independent sites M2A-M2B and M1A-M1B. M2A and M1A flip their shortest and longest bonds during the phase transition connected to the formation of rigid rods and decollement of the inter-rod spaces.

The asphericity parameter of coordination distortion is lower for M3 in β-$Pb_3Bi_2S_6$ than it was in lillianite structure (Figure S2b), whereas all other coordinations, save M1A, have larger values testifying for larger distortion of this kind in the high-pressure polymorph, connected with the last distortion parameter, the volume distortion (Figure S2c). Together with distortions in lillianite and β-$Pb_3Bi_2S_6$, we indicated on Figure S2c the values for four ideal coordination types with CN8 (Archimedean and maximum volume square antiprism) or CN7 (split octahedron and maximum volume split octahedron) (Makovicky and Balic-Zunic 1998). We can see that M3 coordination fits well with the values for square antiprism both in lillianite and in β-$Pb_3Bi_2S_6$. For CN7 coordinations, the values fall in the range of ideal split octahedron

rather than monocapped trigonal prism (volume distortion = 0.1590), which is a typical description of CN7 coordinations (e.g. Berlepsch et al. 2001b). The values again correlate with those of asphericity, M1A having the lowest volume distortion (highest volume efficiency) and M2B the highest distortions of both types. In lillianite, M1 and M2 had very small volume distortions, as well as asphericities and approached well ideal octahedron (Figures 3b and 3c). A general conclusion that comes out from the present data is that most of coordinations increase their distortions on phase transition. On further increase of pressure, only their eccentricity decreases (Figure S2a), testifying for the main compressional mechanism in β-$Pb_3Bi_2S_6$. It should be mentioned, however, that M1A coordination stands out as very regular with even a negligible amount of eccentricity that it keeps throughout the investigated range of pressures.

The volumes of coordination polyhedra of Pb and Bi (Table S2 and S3 in the *Supplementary material* section) in dependence on pressure are represented in Figure 5. A difference between their evolution with *P* is evident: while in M1 (A and B) and M2 (A and B), in the β-$Pb_3Bi_2S_6$ structure, the polyhedral volumes decrease with a similar trend as observed for their "parent" sites in lillianite, M3 volume decreases with a clearly slower trend than M3 in lillianite (Figure 5). This is due to its special position in the structure, on the combination plane of the (010) slabs (Figure 1). The main compression of the structure occurs in diminishing the spaces between the rigid rods and thus highly affecting the volumes of all other coordination polyhedra but M3, that shows the lowest variations.

Twinning and de-twinning in lillianite under high-pressure. In the present study, the observed splitting of reflections of β-$Pb_3Bi_2S_6$ resembles a pseudomerohedral twin (Friese and Grzechnik 2014; Figure S1b in the *Supplementary material* section). One can observe a rotation of the crystal lattices of the two twin domains relative to each other by a small angle around the [001]. During decompression, a de-twinning process occurs together with the restoration of the structure of the original single lillianite crystal (Figure S2c in *Supplementary material* section). As in phase transition the symmetry of the low-

pressure form (*Bbmm*) changes to its sub-group (*Pbnm*) in the high-pressure polymorph, one would expect a merohedral type of twinning (Friese and Grzechnik, 2014) with a perfect overlapping of the two components. On the contrary, in the H*P* lillianite they are rotated relatively to each other. As described earlier, the pressure-induced phase transition in lillianite is characterized by splitting of the (010) structural slabs into strongly bonded two-atom layers thick rods and intra-rod spaces crossed by weak bonds. In general, an atomic plane has two arbitrary choices, either making tight bonds or weak bonds with the neighboring planes, thus defining a rod. Propagated through the crystal structure of the lillianite during transition, these two choices would make two mirror-related structures of the high-pressure form. This would produce a merohedral twinning unless an additional effect of the rod rotation were present. In the contact zone of the two twin domains, a compromise structure can be expected and it can be assumed that it retains or mimics the features of the low-pressure polymorph. Both polymorphs have (010) slabs with atomic planes inclined to the boundary (010) planes giving them a repeating fish-bone pattern when looked along the [001] direction (Figure 1). The inclination of the atomic planes to the (010) plane changes on phase transition, as mentioned in discussion of compression mechanism. At 4.9 GPa, in the low-pressure phase just before the phase transition, this angle is 26.45°; in the high-pressure phase at 6.3 GPa, the angle is 31.52°. In β-$Pb_3Bi_2S_6$ at 8.85 GPa, where we could best determine the orientation matrix for the small twin component, the relative rotation of the two crystal lattices amounted to 6.5° that is close to the change of inclination angle upon the phase transition. Starting from the contact zone of the two twin domains, we can see that the only way of saving the structure continuity with each of the twin domains is a rotation of the *a* and *b* axes around [001]. This is necessary to comply with the larger inclination angle of atomic planes in their β-$Pb_3Bi_2S_6$ structures relative to the one present in the lillianite-like transition zone. The rotation of lattices of the two domains relative to their contact zone has to be in opposite sense (clockwise vs. anti-clockwise) and correspond in magnitude to differences between the inclination angles in the L*P* and H*P* lillianite polymorphs.

Anisotropic compression in L*P* and H*P* lillianite structures

The thorough analysis of the structural characteristics of the β-$Pb_3Bi_2S_6$ here proposed explains the compressional anisotropy of the two polymorphs. The *c*-axes of the unit cell is directly related to the archetypal structure in both polymorphs, corresponding to $[011]_{PbS}$ period in lillianite and $[010]_{SnS}$ period in β-$Pb_3Bi_2S_6$ and the structure is constrained in this direction due to the presence of closely spaced mirror planes perpendicular to this direction. This makes it the least compressible direction in the crystal structure. While in the L*P* lillianite we have a relatively homogeneous distribution of strong and weak bonds inside (010) slabs, in the H*P* lillianite the slabs contain tightly bonded rods separated by spaces crossed only by weak bonds and containing LEP. The compression along the slab extensions [100] is larger than their thinning along [010] in lillianite but the situation reverses in β-$Pb_3Bi_2S_6$. This is related to "harmonica behavior" of the structure: a rotation of the rigid rods around their [001] axes as the main response to compression. The angle between the extension of rigid rods in the *a/b* plane of the two adjacent module slabs (see e.g. Figure 1) changes from 63.04° at 6.3 GPa to 62.21° at 20.9 GPa in accordance with the faster compression along the *b* than along the *a* axis.

LEP evolution and the behavior of Pb-Bi sulphosalts at high pressures

This work shows that the stereochemical expression of the LEP of Pb and Bi, both in L*P* and H*P* polymorphs, evaluated by eccentricity of polyhedral coordinations, decreases with increasing pressure as observed in other similar studies (Lundegaard et al. 2005; Olsen et al. 2007, 2008, 2011; Comodi et al. 2019). This applies for both the L*P* and H*P* phases of $Pb_3Bi_2S_6$.

In detail, in the L*P* lillianite structure during compression up to the transition point, the LEP diminishes its expression as the direction of its displacement follows the shortening of the M2 – S1 longest bond (Figure 1a). In the β-$Pb_3Bi_2S_6$, the LEP of M2A moves to the opposite side of the nucleus as compared with the situation in the L*P* structure and increases its displacement from the nucleus; whereas M1A has the lower eccentricity than its "parent" M1 site in lillianite (Figure S2a). The movements of the

coordinating S atoms change the coordination to CN7 split octahedron, but at the same time equalize the bond lengths so that the stereochemical activity of LEP is suppressed in M1A, whereas it strongly increased in all others. It is also interesting that this site has the smallest displacement calculated by AMPLIMODES, below 0.1 Å ($|\Delta|_{M1A}$ = 0.0762, Table 2), whereas all other atoms have displacements over 0.5 Å (e.g. $|\Delta|_{M2A}$ = 0.6243, $|\Delta|_{M2B}$ = 0.9684 and $|\Delta|_{M3}$ = 1.0038, Table 2), so in this respect it plays a role of a "firm point" during the phase transition. The sites M2B and M1B do not flip the LEP during formation of rigid rods. The changes in coordination in their case produce also the largest distortions of coordination polyhedra in β-$Pb_3Bi_2S_6$ (Figure S2).

The increase of the stereochemical activity of LEP during phase transition from the L*P* to the H*P* phase is also observed for heyrovskiite ($Pb_6Bi_2S_9$; Olsen et al. 2011); whereas, galenobismutite ($PbBi_2S_4$) remains in its ambient pressure structure and does not have phase transitions up to 21 GPa (Comodi et al. 2019). The eccentricity of its cationic sites continuously decreases in response to compression (Figure S2a) except M1 (the lowest CN coordination site in galenobismutite) where eccentricity keeps a nearly constant value as *P* increases. In fact, it becomes the one with the highest eccentricity at high pressure. It is worth noting that M1 in galenobismutite is characterized as a pure Bi site, whereas the other two sites were considered mixed Pb/Bi sites (Pinto et al. 2006). Galena (PbS, *Fm*-3*m* space group) with octahedral coordination of atoms and a suppressed stereochemical activity of LEP of Pb undergoes phase transition to an orthorhombic structure at approximately 2.5 GPa with either *Cmcm* (Grzechnik and Friese 2010) or *Pnma* (Bencherif et al. 2011) symmetry and Pb achieves the seven-fold coordination due to stereochemically active LEP of Pb. On the contrary, bismuthinite (Bi_2S_3) has, already at room pressure, Bi atoms with stereochemically active LEP and seven-fold coordination and does not undergo phase transition up to approximately 50 GPa (da Silva et al. 2019).

We can conclude that the Pb-Bi sulphides with more Pb than Bi atoms in the structure, have a behavior of LEP dominated by the former. At low pressures, the stereochemical activity is low to suppressed,

This is the peer-reviewed, final accepted version for American Mineralogist, published by the Mineralogical Society of America.
The published version is subject to change. Cite as Authors (Year) Title. American Mineralogist, in press.
DOI: https://doi.org/10.2138/am-2021-7765. http://www.minsocam.org/

371 which obviously is an unstable state at pressures, high enough, where the structures transform to types
372 that allow a high stereochemical expression of LEP. This does not apply to Bi-dominated compounds
373 that, already at the lowest pressure, acquire the structures with relatively high expression of LEP. An
374 interesting conclusion is that, at least considering sulfides of Pb and Bi, the stable structures (up to several
375 tens of GPa) are those that allow a relatively significant expression of s^2 LEP of cations already at low
376 pressures, in spite of the general tendency that this expression decreases with pressure, different from
377 structures with a weak expression, which show a limited pressure stability. This persistence of LEP under
378 pressure, granted by the structure type, is obviously a property that stabilizes the crystal structure under
379 high-pressures.

380 **Implications**

381 1. Our results challenge the existing assumption that the pressure-induced phase transitions in
382 structures where LEP has a high stereochemical activity are associated with an increase of
383 coordination number and with the coordination polyhedra becoming more regular (Grzechnik,
384 2007) meaning that they produce structures with less stereochemical activity of LEP. The here
385 described cases of Pb-Bi sulphides can be rationalized considering that the coordinations with
386 higher stereochemical activity of LEP more easily bear the pressure induced strain through
387 equalization of bond distances and suppression of LEP.
388 2. While the pseudomerohedral twinning has been associated to high-pressure experiments (King
389 and Prewitt 1982; Kudoh et al. 1986; Posse et al. 2011), de-twinning was rarely observed on
390 decompression (Kaga and Gilman 1969). Recently, the study of de-twinning has become an
391 attractive topic in the study of shape-memory alloys (e.g. Wang et al. 2018; Rößler et al. 2019),
392 materials that are capable of bearing large recoverable elastic strain under loading-unloading
393 (Wang et al. 2018 and references therein). By its characteristics here presented, phase transition
394 of lillianite qualifies itself as a specifically interesting shape-memory material. Further work

devoted to test the likely ability of lillianite to recuperate the original shape not only while unloading (pseudoelasticity), but also while heating above specific critical temperatures (shape-memory effect), would open a new scenario where lillianite might have important applications in several fields such as (i) aerospace, *i.e.* to isolate the micro-vibrations, for low-shock release devices and self-deployable solar sails (Costanza and Tata 2020), and (ii) photovoltaic panels, as shape-memory alloy springs that act as actuators by contracting with great strength and speed when heated and thus changing the position of the solar panel in accordance to the motion of the sun throughout the day (Gasparetto et al. 2021; Degeratu et al. 2021).

3. Sulfosalt structures are interesting due to their similarities with high-pressure silicate phases that likely occur in the inner Earth, with octahedrally coordinated silicon combined with other cations with the same or higher coordination number. In particular, post-perovskite $MgSiO_3$ (Murakami et al. 2004, Oganov and Ono 2004) is the oxide homologue N=1 of the lillianite series with octahedral Si and bicapped trigonal prismatic (or square antiprismatic) Mg polyhedra (Makovicky and Topa 2014); whereas, $CaTi_2O_4$ (Bertaut and Blum 1956; Rogge et al. 1998; Yamanaka et al. 2008) and the high-pressure phase Fe_4O_5 (Lavina et al. 2011; Guignard and Chrichton 2014) are the N=2 and N=3 homologues, respectively.

While, on the one hand, galenobismutite has the calcium-ferrite structure type, like the aluminous phases of the inner Earth, on the other hand, we do not know yet a deep-Earth analogue of β-$Pb_3Bi_2S_6$. However, recent results of the ultra-high P/T behavior of $NaMgF_3$ (Dutta et al. 2019), used as a model system for understanding phase transitions in ABX_3 (e.g. $MgSiO_3$) systems, show a Sb_2S_3-type (stibnite-type) post-post-perovskite ABX_3 phase at 58 GPa, which remains stable to over 150 GPa and heating to over 2000 K. The β-$Pb_3Bi_2S_6$ structure belongs to the meneghinite homologous series (Olsen et al. 2008), where also stibnite lies; this increases the interest on the phase transition of lillianite in relation to the deep-Earth crystallography. Indeed, a similar

419 sequence of transitions of $NaMgF_3$ is predicted to occur in $MgSiO_3$ system at ultra-high pressures,
420 implying density changes as well as peculiar anisotropic evolution, and thus likely affecting the
421 mineralogy and the dynamic in the deep interior of both the earth and the large extrasolar rocky
422 planets.
423

Acknowledgment

We dedicate this article to Professor Emil Makovicky, who made the major contribution to the crystallography of sulfosalts, on the occasion of his 80th birthday and acknowledgement of the inspiration he gave for our work.
Ross Angel is warmly acknowledged for his help in the absorption correction of the collected data.
The European Synchrotron Facility is acknowledged for allocating beam-time for the experiment ES-723 (main proposer Paola Comodi). Lars Olsen is thanked for the synthesis of the used lillianite crystal. The comments of the anonymous reviewers and the editor Oliver Tschauner significantly helped to increase the quality of the manuscript.

References

Angel, R.J., and Gonzalez-Platas, J. (2013) Absorb-7 and Absorb-GUI for single-crystal absorption corrections. Journal of Applied Crystallography, 46, 252–254.

Balić-Žunić, T. (2007) Use of three-dimensional parameters in the analysis of crystal structures under compression. In: Pressure-Induced Phase Transitions 2007, ed. Grzechnik A., pp. 157-184, Transworld Research Network, Kerala, India. ISBN: 81-7895-272-6.

Balić Žunić, T., and Makovicky, E. (1996) Determination of the Centroid or "the Best Centre" of a Coordination Polyhedron. Acta Crystallographica, B52, 78–81.

Balić Žunić, T., and Vicković, I. (1996) IVTON - Program for the Calculation of Geometrical Aspects of Crystal Structures and Some Crystal Chemical Applications. Journal of Applied Crystallography, 29, 305–306.

Bass, J.D., Liebermann, R.C., Weidner, D.J., Finch, S.J. (1981) Elastic properties from acoustic and volume compression experiments. Physics of the Earth and Planetary Interiors, 25, 140–158.

Bencherif, Y., Boukra, A., Zaoui, A., and Ferhat, M. (2011) High-pressure phases of lead chalcogenides. Materials Chemistry and Physics, 126, 707–710.

Berlepsch, P., Armbruster, T., Makovicky, E., Hejny, C., Topa, D. and Graeser, S. (2001a) The crystal structure of (001) twinned xilingolite, $Pb_3Bi_2S_6$, from Mittal-Hohtenn, Valais, Switzerland. The Canadian Mineralogist, 39, 1653-1663.

Berlepsch, P., Makivicky, E., and Balić Žunić, T., (2001b) The crystal chemistry of meneghinite homologues and related compounds. Neues Jahrbuch für Mineralogie – Monatshefte, 3, 115-135.

Bertaut, E F., and Blum, P. (1956) Détermination de la Structure de Ti_2CaO_4 par la Méthode Self-Consistante d'Approche Directe. Acta Crystallographica, 9, 121-126.

Blessing, R.H. (1995) An empirical correction for absorption anisotropy. Acta Crystallographica Section A, 51, 33–38.

Brown, I.D., Altermatt, D. (1985) Bond-valence parameters obtained from a systematic analysis of the Inorganic Crystal Structure Database. Acta Crystallographica B41, 244–247.

Comodi P., Guidoni F., Nazzareni S., Balić-Žunić, T., Zucchini A., Makovicky E., and Prapapenka V. (2018) A high-pressure phase transition in chalcostibite, $CuSbS_2$. European Journal of Mineralogy, 30(3), 491–505.

Comodi, P., Zucchini. A., Balić-Žunić, T., Hanfland, H., and Collings, I. (2019) The High-pressure Behavior of Galenobismutite, $PbBi_2S_4$: A Synchrotron Single Crystal X-ray Diffraction Study. Crystals, 9, 210.

Costanza, G., and Tata, M.E. (2020) Shape Memory Alloys for Aerospace, Recent Developments, and New Applications: A Short Review. Materials (Basel), 13(8), 1856.

CrysAlisPRO, Oxford Diffraction /Agilent Technologies UK Ltd, Yarnton, England.

Degeratu, S., Subțirelu, G.E., Rotaru, A., Bîzdoacă, N.G., and Rotaru, P. (2021) The electro-mechanical control of element NiTi shape memory alloy strip while bending, based on thermal analysis evidence. Journal of Thermal Analysis and Calorimetry, 143, 3805–3815.

Dutta, R., Greenberg, E., Prakapenka, V.B., and Duffy, T.S. (2019) Phase transitions beyond post-perovskite in $NaMgF_3$ to 160 GPa. PNAS, 116 (39), 19324-19329.

Farrugia, L.J. (1999) WinGX suite for small-molecule single-crystal crystallography. Journal of Applied Crystallography, 32, 837–838.

Friese. K., and Grzechnik, A. (2014) Twinning and pseudosymmetry under high-pressure. Zeitschrift für Kristallographie, 229(2), 158–168.

Gasparetto, V.M.L., Kanevsky, M., and Jiang, X.X. (2021) Solar Panel Deployment Using Shape Memory Alloy Actuator. AIAA Scitech 2021 Forum, Session: Adaptive Spacecraft Structures II, 11–15 & 19–21 January 2021 VIRTUAL EVENT. AIAA 2021-1608.

Gonzalez-Platas, J., Alvaro, M., Nestola, F., and Angel, R.J. (2016) EosFit7-GUI: A new GUI tool for equation of state calculations, analyses. and teaching. Journal of Applied Crystallography, 49, 1377–1382.

Grzechnik, A. (2007) Stereochemistry of lone electron pairs in inorganic materials at high pressure. In: Pressure-Induced Phase Transitions 2007, ed. Grzechnik A., pp. 185-213, Transworld Research Network, Kerala, India. ISBN: 81-7895-272-6.

Grzechnik, A., and Friese, A. (2010) Pressure-induced orthorhombic structure of PbS. Journal of Physics: Condensed Matter, 22, 095402.

Guignard, J., and Crichton, W.A. (2014) Synthesis and recovery of bulk Fe_4O_5 from magnetite, Fe_3O_4. A member of a self-similar series of structures for the lower mantle and transition zone. Mineralogical Magazine, 78(2), 361–371.

Hammersley, A.P.; Svensson, S.O.; Hanfland, M.; Fitch, A.N.; Hausermann, D. (1996) Two-dimensional detector software: From real detector to idealized image or two-theta scan. High Pressure Research, 14, 235–245.

Hübschle, C.B., Sheldrick, G.M., and Dittrich, B. (2011) ShelXle: a Qt graphical user interface for SHELXL. Journal of Applied Crystallography, 44, 1281–1284.

Kaga, H., and Gilman, J.J. (1969) Twinning and Detwinning in Calcite. Journal of applied physics, 40, 3196–3207.

Kanno, S., Imamura, Y., and Hada, M. (2019) Alternative materials for perovskite solar cells from materials informatics. Physical Review Materials, 3, 075403.

King, H.E., and Prewitt, C. (1982) High-pressure and high-temperature polymorphism of iron sulfide (FeS). Acta Crystallographica B38, 1877–1887.

Kudoh, Y., Takeda, H., and Arashi, H. (1986) In situ determination of crystal structure for high-pressure phase of ZrO_2 using a diamond anvil and single crystal X-ray diffraction method. Physics and Chemistry of Minerals, 13, 233–237.

Lavina, B., Dera, P., Kim, E., Meng, Y., Downs, R.T., Weck, P.F., Sutton, S.R. and Zhao, Y. (2011) Discovery of the recoverable high-pressure iron oxide Fe_4O_5. Proceedings of the National Academy of Sciences, USA, 108, 17281–17285.

Lundegaard, L.F., Makovicky, E., Boffa-Ballaran, T., and Balić-Žunić, T. (2005) Crystal structure and cation lone electron pair activity of Bi_2S_3 between 0 and 10 GPa. Physics and Chemistry of Minerals 32, 578–584.

Makovicky E. (1977) Chemistry and crystallography of the lillianite homologous series. Part III: Crystal chemistry of lillianite homologues. Related phases. Neues Jahrbuch für Mineralogie Abhandlungen 131, 187–207.

548

549 Makovicky, E., and Balić-Žunić, T. (1998) New measure of distortion for coordination polyhedra. Acta
550 Crystallographica B54, 766-773.

551

552 Makovicky, E., and Topa, D. (2014) Lillianites and andorites: new life for the oldest homologous series
553 of sulfosalts. Mineralogical Magazine, 78(2), 387–414.

554

555 Momma, K., and Izumi, F. (2011). VESTA 3 for three-dimensional visualization of crystal, volumetric
556 and morphology data. Journal of Applied Crystallography, 44, 1272-1276.

557

558 Murakami, M., Hirose, K., Kawamura, K., Sata, N., and Ohishi, Y. (2004) Post-Perovskite Phase
559 Transition in $MgSiO_3$. Science, 304(5672), 855–858.

560

561 Oganov, A.R., Ono, S. (2004) Theoretical and experimental evidence for a post-perovskite phase of
562 $MgSiO_3$ in Earth's D'' layer. Nature 430, 445–448.

563

564 Olsen, L.A., Balić-Žunić, T., Makovicky, E., Ullrich, A., and Miletich, R. (2007) Hydrostatic
565 compression of galenobismutite ($PbBi_2S_4$): elastic properties and high-pressure crystal chemistry.
566 Physics and Chemistry of Minerals 34(7), 467–475.

567

568 Olsen, L.A., Balić-Žunić, T., and Makovicky, E. (2008) High-Pressure Anisotropic Distortion of
569 $Pb_3Bi_2S_6$: a Pressure-Induced, Reversible Phase Transition with Migration of Chemical Bonds. Inorganic
570 Chemistry, 47, 6756–6762.

571

572 Olsen, L.A., Friese, K., Makovicky, E., Balić-Žunić, T., Morgenroth, T., and Grzechnik, A. (2011)
573 Pressure induced phase transition in $Pb_6Bi_2S_9$. Physics and Chemistry of Minerals, 38, 1–10.

574

575 Olvera, A., Shi, G., Djieutedjeu, H., Page, A., Uher, C., Kioupakis, E., and Poudeu, P.F.P. (2015)
576 $Pb_7Bi_4Se_{13}$: A Lillianite Homologue with Promising Thermoelectric Properties. Inorganic Chemistry, 54,
577 746–755.

578

Orobengoa, D., Capillas, C., Aroyo, M.I., and Perez-Mato, J.M. (2009) AMPLIMODES: symmetry-mode analysis on the Bilbao Crystallographic Server. Journal of Applied Crystallography 42, 820–833.

Pinto, S., Balić-Žunić, T., Garavelli, A., Makovicky, E., and Vurro, F. (2006) Comparative crystal-structure study of Ag-free lillianite and galenobismutite from Vulcano, Aeolian Islands, Italy. The Canadian Mineralogist, 44, 159–175.

Posse, J.M., Friese, K., and Grzechnik, A. (2011) Structural stability of $BaMF_4$ (M ¼ Zn, Mg, and Mn) at high-pressures. Journal of Physics: Condensed Matter, 23, 215401.

Rogge, M.P., Caldwell, J.H., Ingram, D.L., Green, C.E., Geselbracht, M.J., and Siegrist, T. (1998) New Synthetic Route to Pseudo-Brookite-Type $CaTi_2O_4$. Journal of Solid State Chemistry, 141, 338-342.

Rößler, S., Koz, C., Wang, Z., Skourski, Y., Doerr, M., Kasinathan, D., Rosner, H., Schmidt, M., Schwarz, U., Rößler, U.K., and Wirth, S. (2019) Two types of magnetic shape-memory effects from twinned microstructure and magneto-structural coupling in $Fe_{1+y}Te$. PNAS, 116 (34), 16697-16702.

da Silva, E.L., Skelton, J.M., Rodríguez-Hernández, P., Muñoz, A., Martínez-García, D., and Manjón F.J. (2019) Theoretical study of phase transitions in Sb_2S_3, Bi_2S_3 and Sb_2Se_3 under compression. arXiv: Materials Science.

Takagi, J., and Takéuchi, Y. (1972) The crystal structure of lillianite. Acta Crystallographica, B28, 649–651.

Wallace, S.K., Svane, K.L., Huhn, W.P., Zhu T., Mitzi, D.B., Blum, V., and Walsh, A. (2017) Candidate photoferroic absorber materials for thinfilm solar cells from naturally occurring minerals: enargite, stephanite, and bournonite. Sustainable Energy Fuels, 1, 1339.

Wang, X., Kustov, S., and Humbeeck, J.V. (2018) A short review on the microstructure, transformation behavior and functional properties of NiTi shape memory alloys fabricated by selective laser melting. Materials, 11(9), 1683.

611 Yamanaka, T, Uchida, A., and Nakamoto, Y. (2008) Structural transition of post-spinel phases $CaMn_2O_4$,
612 $CaFe_2O_4$, and $CaTi_2O_4$ under high pressures up to 80 GPa. American Mineralogist, 93, 1874-1881.
613

614 **List of figure captions**

615

616 **Figure 1** (a) Lillianite crystal structure projected in the *ab* plane. Yellow, gray and pink denote S, Pb
617 and Bi, respectively. The slab thickness is shown by the number of octahedra in the row across a slab
618 (purple octahedra), defining the homologue order ($N = 4$), with a [PbS_{6+2}] bicapped trigonal prism in
619 gray on the slab boundary. The mirror plane (*m*) perpendicular to the *b*-axis is also shown as solid line.
620 (b) β-$Pb_3Bi_2S_6$ crystal structure projected in the *ab* plane. Colors are according to (a) and the *n* glide
621 planes, appearing in the place of *m* perpendicular to the *b*-axis, are shown as dashed-dotted lines. The
622 two of the rigid rods in β-$Pb_3Bi_2S_6$ are shaded and, for comparison, a corresponding part in the crystal
623 structure of lillianite. The crystal structures was were drawn by VESTA software (Momma and Izumi
624 2011).

625

626 **Figure 2** Evolution of the unit cell volume and unit cell parameters with *P*, fitted by the third-order BM
627 EOSs. (a) *V* (black); (b) *a* (red), *b*/2 (blue), *c**2 (green). Full circles and triangles refer to lillianite and β-
628 $Pb_3Bi_2S_6$, respectively. Data during decompression are shown as stars. Data for *lill2* from Olsen et al.
629 (2008) are shown as empty symbols.

630

631 **Figure 3** Confidence ellipses at 68.3% confidence level for the *V* vs. *P* BM3 EoS of lillianite and β-
632 $Pb_3Bi_2S_6$. For the β-$Pb_3Bi_2S_6$ the bulk modulus and its first derivative were calculated at 4.9 GPa, in order
633 to a direct comparison with data by Olsen et al (2008).

634

635 **Figure 4** The displacements of atomic sites of β-$Pb_3Bi_2S_6$ at 6.3 GPa relative to their positions in the
636 low-pressure lillianite. *a* axis vertical, *b* horizontal and *c* perpendicular to the projection plane. The atoms
637 at two different *z* levels are differently shaded. The displacements are indicated by blue color for cation

638 sites and green for S sites. All displacements are parallel to (001) plane. Yellow shading indicates one of
639 the rigid rods. A 2_1 axis runs through the center of the rod perpendicular to the plane of projection.
640
641 **Figure 5** Volumes of coordination polyhedra at various pressures. Symbols and colors are according to
642 the legend; the empty symbols are data during decompression.
643

This is the peer-reviewed, final accepted version for American Mineralogist, published by the Mineralogical Society of America.
The published version is subject to change. Cite as Authors (Year) Title. American Mineralogist, in press.
DOI: https://doi.org/10.2138/am-2021-7765. http://www.minsocam.org/

644 **Deposit Items**

645

646 **Table S1** Relation of atomic site labeling in this work to Olsen et al. (2008) labeling.

647

648 **Table S2** Bond distances, average bond distances and volumes of coordination polyhedra in lillianite at
649 various pressures.

650

651 **Table S3** Bond distances, average bond distances and volumes of coordination polyhedra in β-$Pb_3Bi_2S_6$
652 at various pressures.

653

654 **Figure S1** Collected data extraction and unit cells used for reflection indexing at 1.74 GPa (single
655 lillianite crystal) (a), 6.30 GPa (twinned β-$Pb_3Bi_2S_6$) (b) and 2.13 GPa during decompression (the
656 detwinned single lillianite crystal) (c).

657

658 **Figure S2.** Eccentricities of coordination polyhedra at various pressures. In red, data for coordinations
659 in galenobismutite (Comodi et al. 2019): squares M1 (CN6), circles M2 (CN7), triangles M3 (CN8) (a);
660 asphericities of coordination polyhedra at various pressures (b); volume distortion of coordination
661 polyhedra at various pressures. Squares represent M1 in lillianite (black), M1A (blue) and M1B (green)
662 in β-$Pb_3Bi_2S_6$; circles M2 in lillianite (black), M2A (blue) and M2B (green) in β-$Pb_3Bi_2S_6$; triangles M3
663 in lillianite (black) and β-$Pb_3Bi_2S_6$ (blue). The empty symbols are data during decompression. The dashed
664 horizontal lines indicate values for the regular maximum-volume square antiprism (0.0351),
665 Archimedean square antiprism (0.0535), maximum-volume split octahedron (0.0790) and simple split
666 octahedron (0.1333) (c).

667

668 **Bond valences.** Details on the used procedure and obtained results of the bond valences calculation.

669

670 The refined crystal structures, the *hkl* Miller indices of the indexed reflections as well as the Fo^2 (squared

671 observed F values) and Fc^2 (squared calculated F values) are deposited in the *cif* file at the publisher.

This is the peer-reviewed, final accepted version for American Mineralogist, published by the Mineralogical Society of America.
The published version is subject to change. Cite as Authors (Year) Title. American Mineralogist, in press.
DOI: https://doi.org/10.2138/am-2021-7765. http://www.minsocam.org/

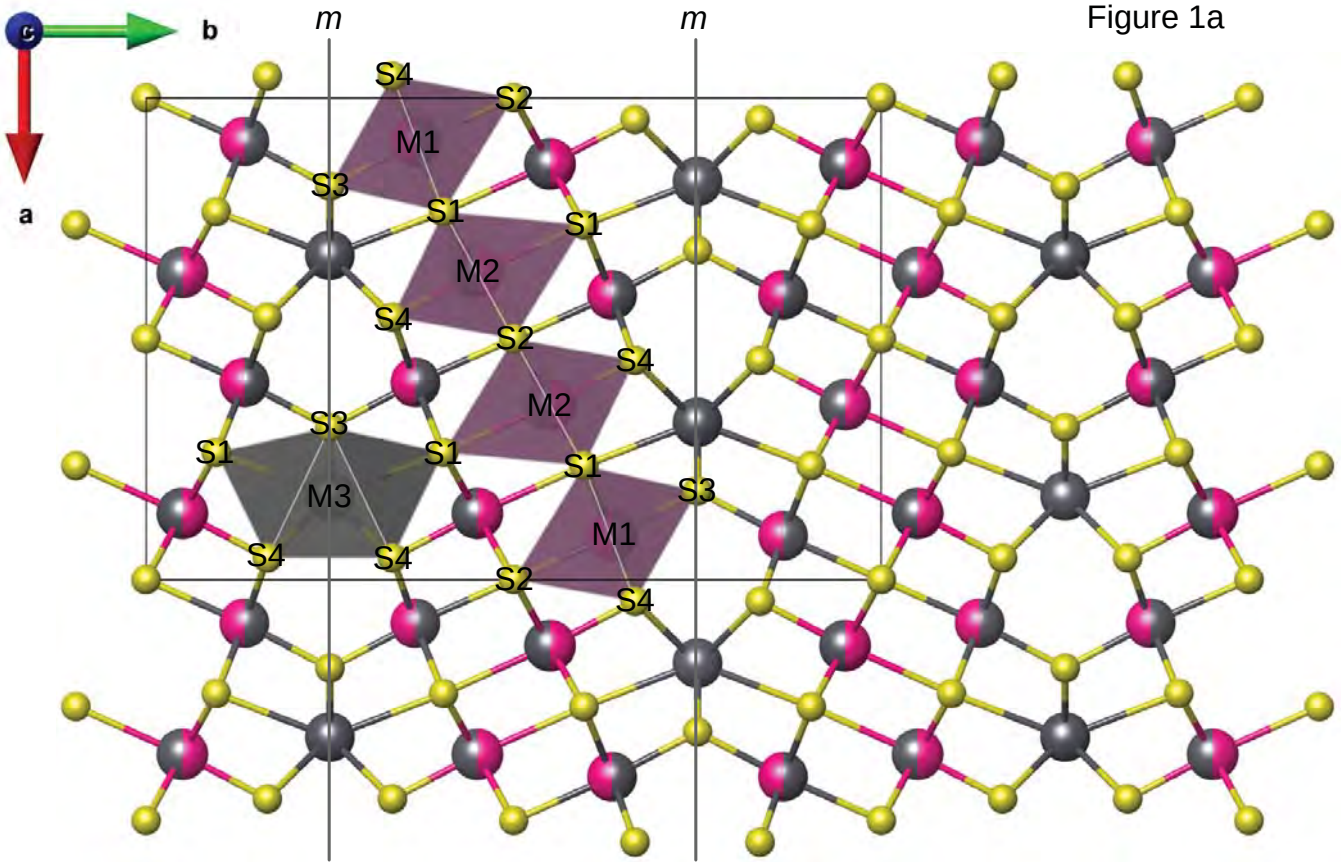

Figure 1a

This is the peer-reviewed, final accepted version for American Mineralogist, published by the Mineralogical Society of America.
The published version is subject to change. Cite as Authors (Year) Title. American Mineralogist, in press.
DOI: https://doi.org/10.2138/am-2021-7765. http://www.minsocam.org/

Figure 1b

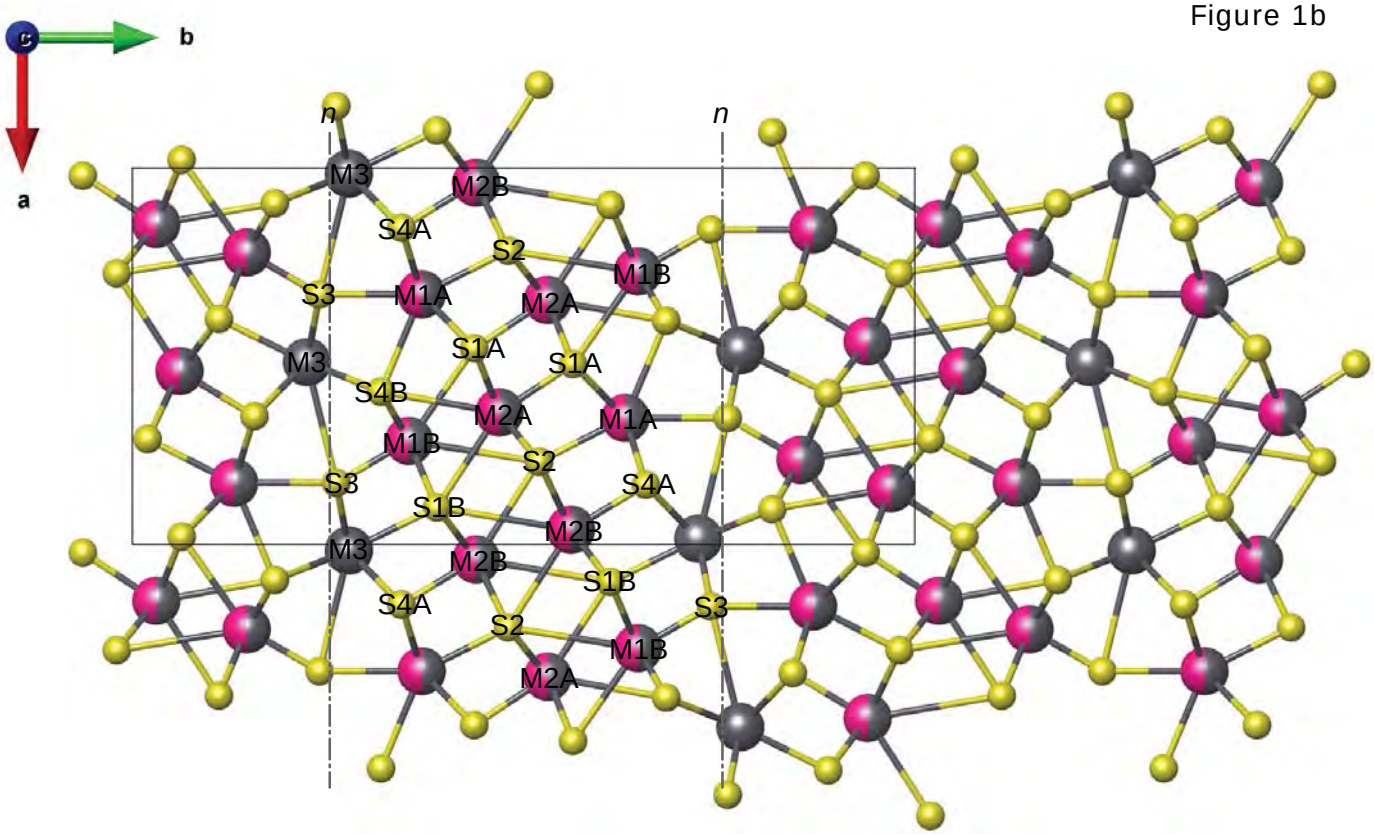

This is the peer-reviewed, final accepted version for American Mineralogist, published by the Mineralogical Society of America.
The published version is subject to change. Cite as Authors (Year) Title. American Mineralogist, in press.
DOI: https://doi.org/10.2138/am-2021-7765. http://www.minsocam.org/

Figure 2a

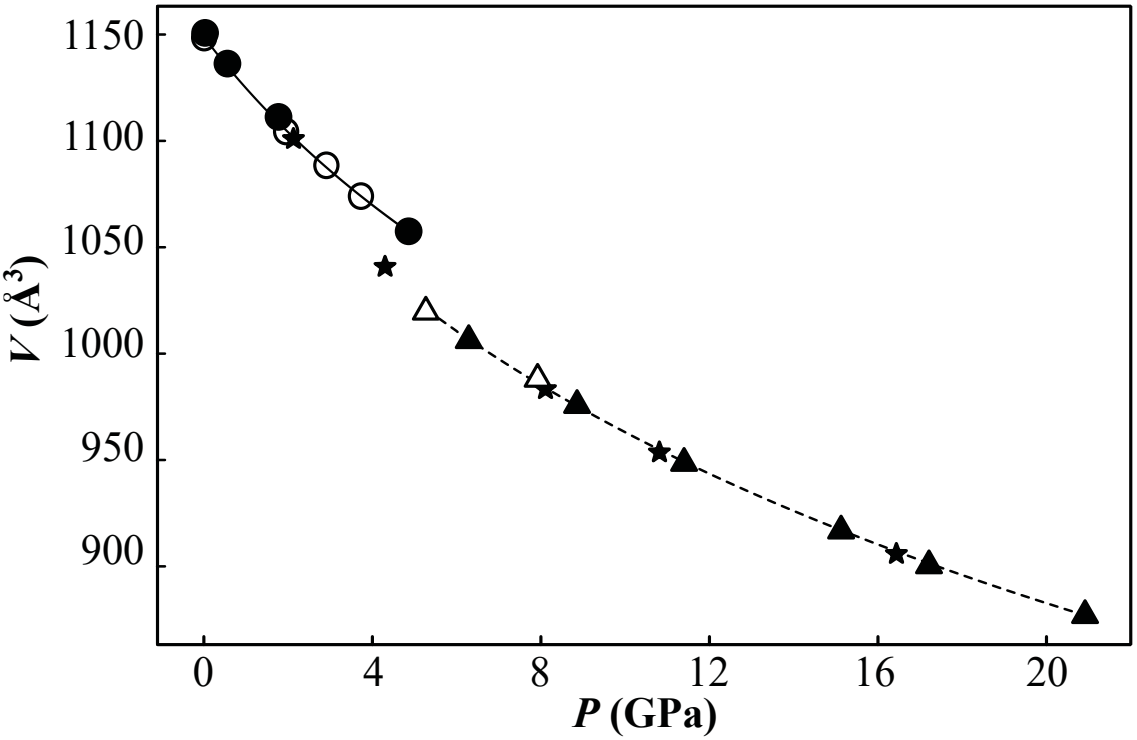

This is the peer-reviewed, final accepted version for American Mineralogist, published by the Mineralogical Society of America.
The published version is subject to change. Cite as Authors (Year) Title. American Mineralogist, in press.
DOI: https://doi.org/10.2138/am-2021-7765. http://www.minsocam.org/

Figure 2b

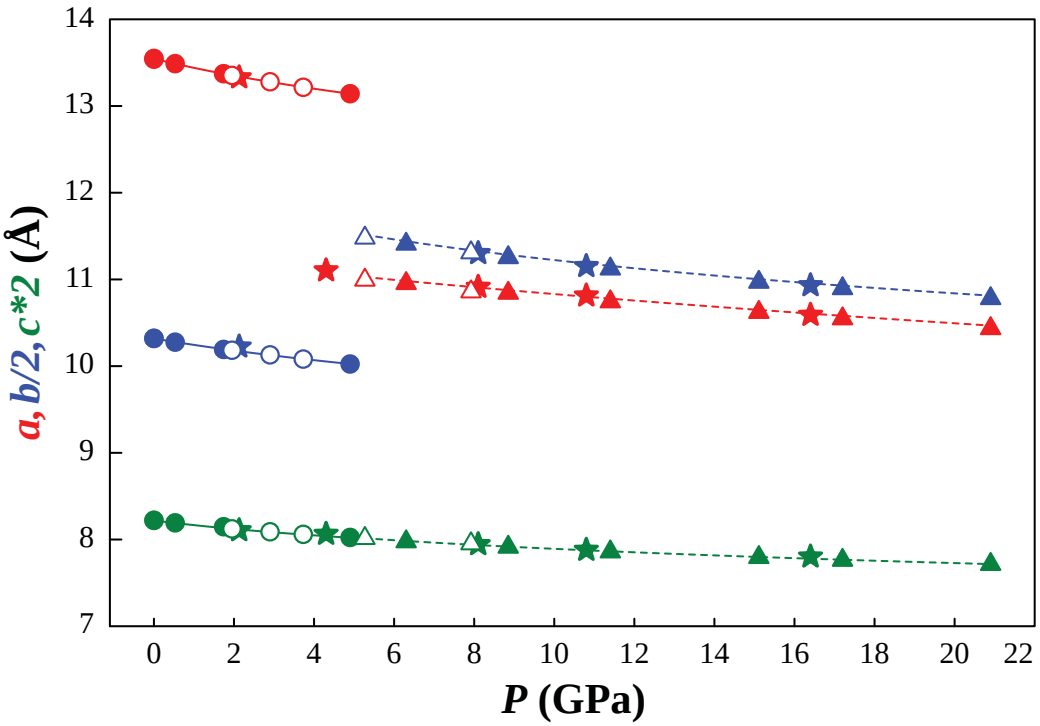

This is the peer-reviewed, final accepted version for American Mineralogist, published by the Mineralogical Society of America.
The published version is subject to change. Cite as Authors (Year) Title. American Mineralogist, in press.
DOI: https://doi.org/10.2138/am-2021-7765. http://www.minsocam.org/

Figure 3

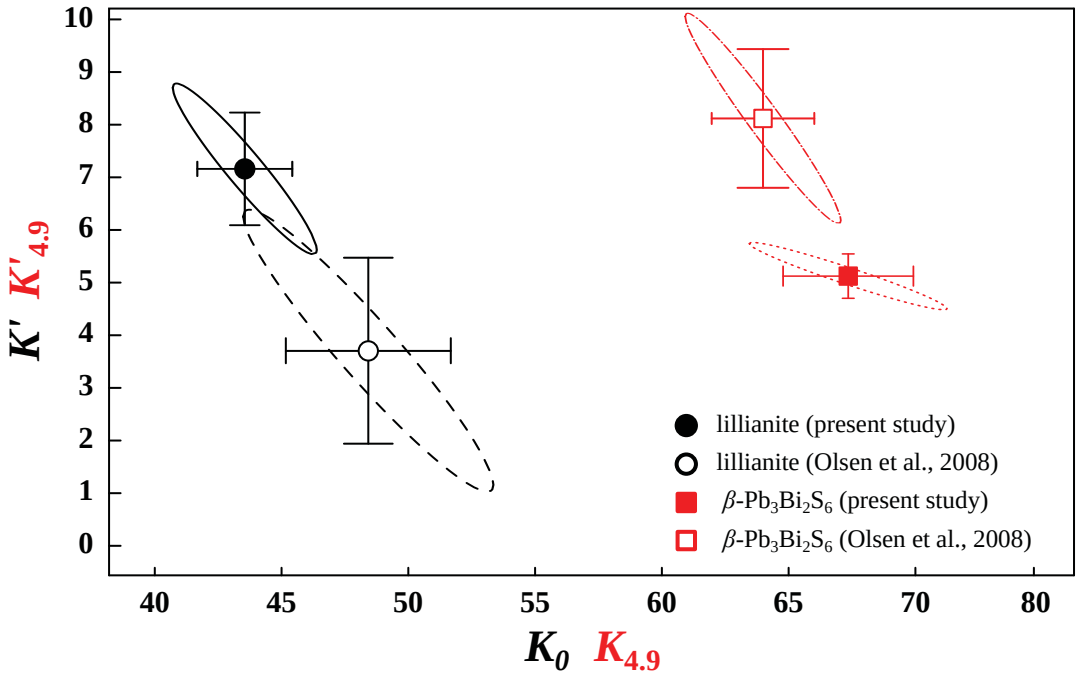

This is the peer-reviewed, final accepted version for American Mineralogist, published by the Mineralogical Society of America.
The published version is subject to change. Cite as Authors (Year) Title. American Mineralogist, in press.
DOI: https://doi.org/10.2138/am-2021-7765. http://www.minsocam.org/

Figure 4

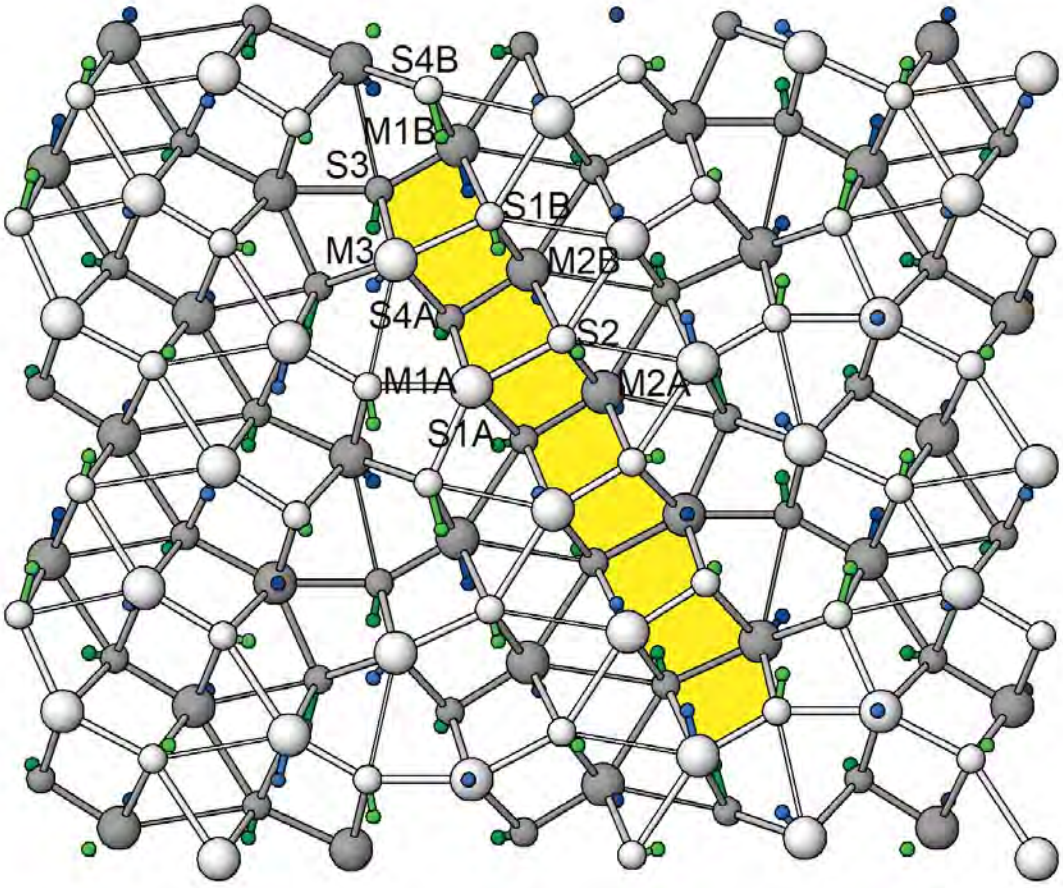

Figure 5

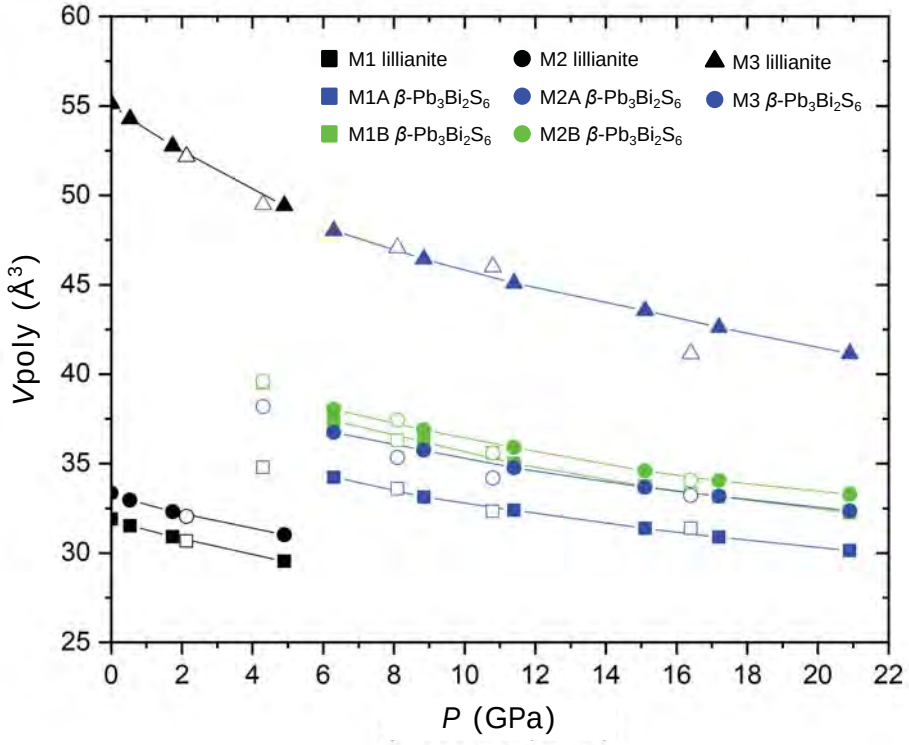

This is the peer-reviewed, final accepted version for American Mineralogist, published by the Mineralogical Society of America.
The published version is subject to change. Cite as Authors (Year) Title. American Mineralogist, in press.
DOI: https://doi.org/10.2138/am-2021-7765. http://www.minsocam.org/

Table 1 Results of the EoS elaboration for lillianite and β-$Pb_3Bi_2S_6$. Cell parameters (*a*, *b* and *c*) and cell volumes (*V*) are given in Å and Å^3, respectively; whereas moduli (K and M) are in GPa. First derivatives of bulk and axial moduli are given as K' and M'. Results of the EoS calculation from Olsen et al. (2008) are also listed.

	lillianite		β-lillianite			
	present work	Olsen et al. (2008)	present work		Olsen et al. (2008)	
V_0	1149.3(9)	1148.5(3)	$V_{4.9}$	1027(1)	$V_{4.9}$	1028.8(7)
K_0	44(2)	48.4(1.7)	$K_{4.9}$	67(3)	$K_{4.9}$	63.8(3)
K'	7(1)	4.0(1.3)	K'	5.1(4)	K'	8.1(1.0)
a_0	13.546(4)		$a_{4.9}$	11.043(7)		
M_0	118(5)		$M_{4.9}$	242(12)		
M'	21(3)		M'	8(1)		
b_0	20.638(5)		$b_{4.9}$	23.085(8)		
M_0	130(6)		$M_{4.9}$	145(4)		
M'	19(3)		M'	16.0(7)		
c_0	4.1115(3)		$c_{4.9}$	4.028(2)		
M_0	139(12)		$M_{4.9}$	242(5)		
M'	31(10)		M'	29(1)		

This is the peer-reviewed, final accepted version for American Mineralogist, published by the Mineralogical Society of America.
The published version is subject to change. Cite as Authors (Year) Title. American Mineralogist, in press.
DOI: https://doi.org/10.2138/am-2021-7765. http://www.minsocam.org/

Table 2 The displacements of atomic sites at 4.9 GPa and 6.3 GPa relative to those at 1 MPa, as calculated by AMPLIMODES (Orobengoa et al. 2009). Δ_x, Δ_y and Δ_z are given in relative units. $|\Delta|$ is the absolute distance given in Å.

Lillianite at 4.9 GPa					β-$Pb_3Bi_2S_6$ at 6.3 GPa				
Site	Δ_x	Δ_y	Δ_z	$\|\Delta\|$	Site	Δ_x	Δ_y	Δ_z	$\|\Delta\|$
M1	-0.0026	0	0.0000	0.0822	M1B	-0.1147	0.0132	0.0000	1.5304
M1’	-0.0026	0	0.0000	0.0175	M1A	-0.0014	0.0037	0.0000	0.0762
M2	-0.0028	-0.0018	0.0000	0.0564	M2B	-0.0707	0.0135	0.0000	0.9684
M2’	-0.0028	0.0018	0.0000	0.0097	M2A	0.0401	0.0167	0.0000	0.6243
M3	0.0022	0	0.0000	0.0059	M3	-0.0640	-0.0273	0.0000	1.0038
S1	-0.0005	0.0025	0.0000	0.0511	S1B	-0.0814	0.0101	0.0000	1.0887
S1’	-0.0005	-0.0025	0.0000	-0.0285	S1A	-0.0141	0.0311	0.0000	0.6511
S2	0	0	0.0000	0.0182	S2	0.0342	-0.0196	0.0000	0.5970
S3	-0.0028	0	0.0000	0.0762	S3	-0.0940	-0.0070	0.0000	1.2433
S4	-0.0048	0.001	0.0000	0.0677	S4A	-0.0356	-0.0106	0.0000	0.5139
S4’	-0.0048	-0.001	0.0000	0.1163	S4B	-0.1181	-0.0159	0.0000	1.5845